https://doi.org/10.3311/PPee.13454

Periodica Polytechnica Electrical Engineering and Computer Science, 63(2), pp. 77–84, 2019

Theoretical Framework of Radiation Force in Surface Acoustic Waves for Modulated Particle Sorting

Gergely Simon[1], Marco A. B. Andrade[2], Marc P. Y. Desmulliez[1], Mathis O. Riehle[3], Anne L. Bernassau[1*]

[1] School of Engineering and Physical Sciences, Institute of Signals, Sensors and Systems, Heriot-Watt University, Earl Mountbatten Building First Gait, Edinburgh EH14 4AS, United Kingdom
[2] Institute of Physics, University of São Paulo, São Paulo, Rua do Matão 1371, Brazil
[3] Institute of Molecular Cell and Systems Biology, Centre for Cell Engineering, University of Glasgow, Joseph Black Building, University Place, Glasgow, G12 8SU, United Kingdom
* Corresponding author, e-mail: A.Bernassau@hw.ac.uk

Received: 14 November 2018, Accepted: 14 January 2018, Published online: 28 March 2019

Abstract

Sorting specific target entities from sample mixtures is commonly used in many macroscale laboratory processing, such as disease diagnosis or treatment. Downscaling of sorting systems enables less laboratory space and fewer quantities of sample and reagent. Such lab-on-a-chip devices can perform separation functions using passive or active sorting methods. Such a method, acoustic sorting, when used in microfluidics, offers contactless, label-free, non-invasive manipulation of target cells or particles and is therefore the topic of active current research. Our phase-modulated sorting technique complements traditional time-of-flight techniques and offers higher sensitivity separation using a periodic signal. By cycling of this periodic signal, the target entities are gradually displaced compared to the background debris, thereby achieving sorting. In this paper, we extend the knowledge on phase-modulated sorting techniques. Firstly, using numerical simulations, we confirm the sorting role of our proposed primary acoustic radiation force within surface wave devices. Secondly, a threefold agreement between analytical, numerical and experimental sorting trajectories is presented.

Keywords

particle sorting, acoustic tweezers, acoustic radiation force, surface acoustic waves, phase-modulation

1 Introduction

The miniaturization of macroscale laboratory systems into Lab-on-a-chip (LoC) devices, enabling the development of compact portable systems, offers a twofold advantage. The required amount of targets and reagents is reduced and new particle handling methods are made possible due to the nonlinear scaling of various forces [1]. As the volume forces, such as gravity or most field forces, are dominated by the surface forces, new phenomena that include diffusion [2], laminar flow profile [3] or short thermal response time [4] can be utilized.

An important sample processing step within LoC devices is sorting [5]. Removal of unwanted entities within a sample can aid detection of target biomarkers, thus facilitating diagnosis of diseases, such as cancer [6] or sepsis [7]. Similarly, filtering harmful entities from body fluids can aid disease treatment. In addition, LoC devices can also be useful in forensic applications, where enrichment of DNA fragments within low amounts of samples can be used directly at the crime scene [8]. Yet the major challenges of achieving high throughputs and/or sorting purity still remain [9].

Available microfluidic sorting methods are usually grouped into four categories: passive devices, bead-based methods, fluorescence-activated sorting strategies (FACS), and label-free active methods [5, 10]. The passive devices are the simplest to design and operate and offer a low-cost solution. However, passive techniques lack reconfigurability to suit various target entities and are usually restricted to separate based on size or compressibility [11]. Due to the limitations of passive devices and the serial processing feature of FACS methods [12], active sorting techniques are widely investigated as possible alternatives.

Active sorting methods [13] utilize an external field to manipulate particles. With direct active methods, the

Cite this article as: Simon, G., Andrade, M. A. B., Desmulliez, M. P. Y., Riehle, M. O., Bernassau, A. L. "Theoretical Framework of Radiation Force in Surface Acoustic Waves for Modulated Particle Sorting", Periodica Polytechnica Electrical Engineering and Computer Science, 63(2), pp. 77–84, 2019. https://doi.org/10.3311/PPee.13454

target particles are selectively displaced laterally based on a field dependent physical property (such as permeability) and collected at the target outlet of the device. Similarly, beads, which have strong dependence on the external field and specific surface binding properties, can be attached to the target cells. The field exerts large force on the beads, which drag target cells with them. Active methods offer reconfigurability over passive devices [14] and can be adjusted to various target populations. Acoustic techniques are especially favored due to their non-contact, non-invasive, label-free properties [15].

In all acoustic fields, microparticles suspended in the media experience a so-called primary radiation force due to time-averaged second order effects [16, 17]. In standing waves, the force moves the particles towards either the nodes or antinodes of the pressure, based on the acoustic contrast factor that depends on the density and compressibility of the particles and the liquid [16]. In most cases, the contrast factor is positive, forcing the particles to collect at the pressure nodes. Although standing waves in surface wave devices are similar to bulk standing waves, we proposed a different radiation force describing the effect of standing surface acoustic waves on particles [18]. The interplay of the acoustic radiation force and hydrodynamic forces can be used for sorting.

Our sorting method utilizes an active sorting technique based on phase modulated acoustic standing waves. The particles are periodically refocused at their stable trapping location at the nodes. With our technique a lower size ratio can then be successfully used to separate particles as opposed to time-of-flight methods [19].

The structure of the paper is as follows: in Section 2 we discuss the radiation force equation proposed in our previous work [18] for the horizontal direction in a standing surface acoustic wave and expand our research with description of the force in the vertical direction within the microchannel. We describe a finite element model and its implementation in COMSOL to verify the proposed horizontal force equation. As the vertical force is a result of pure travelling waves, it cannot be modeled using the Gorkov potential approach [17, 21]. In Section 3 we introduce our particle sorting technique. Section 4 introduces the analytical trajectory equation, an extension of the finite element model to simulate these trajectories and our experimental setup. Agreement between analytical, simulation and experimental particle trajectories is demonstrated for density-based sorting in phase-modulated fields.

2 Proposed primary acoustic radiation force in surface acoustic wave devices

In bulk acoustic wave devices, the primary acoustic radiation force in a standing wave field, $F_{\mathrm{rad},y}$, along the y-direction of the flow (Fig. 1) is usually given as

$$F_{\mathrm{rad},y} = c_{\mathrm{ac}} \sin\left(2k_y y\right)$$
$$c_{\mathrm{ac}} = E_{\mathrm{ac}} V_{\mathrm{p}} \Phi_{\mathrm{AC}} k \tag{1}$$

where E_{ac} is the acoustic energy density, V_{p} the particle volume, Φ_{AC} the acoustic contrast factor, and k the wavenumber [16]. The radiation force collects particles with positive contrast factor at the pressure nodes, whereas particles with negative contrast are gathered at the pressure antinodes. Although the primary acoustic radiation force in surface acoustic wave devices has a similar form as of Eq. (1), the acoustic contrast factor is different.

A typical microfluidic surface acoustic wave device is illustrated in Fig. 1. The device consists of two interdigitated transducers (IDTs) on top of a lithium-niobate ($LiNbO_3$) substrate and a polydimethylsiloxane (PDMS) microchannel. When excited by a sinusoidal wave, each IDT emits a surface acoustic wave that travels in opposite directions along the substrate. As the surface of the substrate is unbounded, the wave travels towards the PDMS microchannel with minimal attenuation. Reaching the channel filled with water, the surface wave is partially radiated into the liquid at an angle and partially travels on the surface as a leaky surface acoustic wave (LSAW). The angle of propagation within the water is given by the boundary condition at the water-lithium niobate interface: the projection of the wave vector of the bulk acoustic wave (BAW) must equal the wavenumber of the surface wave, $k_y = k_{\mathrm{s}} = 2\pi f / c_{\mathrm{s}}$ and therefore $\theta_{\mathrm{r}} = \sin^{-1}\left(c_0 / c_{\mathrm{s}}\right)$ where c_0 and c_{s} are the wave speeds

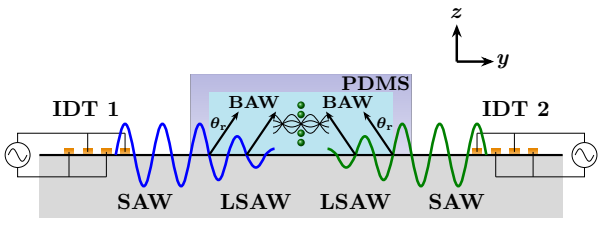

Fig. 1 Schematic of the surface acoustic wave sorting device with the PDMS microchannel bonded on top. The IDTs launch surface waves, which are converted to leaky surface waves at the water/lithium niobate interface, radiating two travelling bulk acoustic waves into the fluid. The boundary condition for the apparent wavenumbers at the surface gives the radiation angle, θ_r. The combination of the two travelling waves forms a standing wave, that traps particles at the pressure nodes. An expanded version of the figure illustrating phase modulation and the resulting trapping positions can be found in [18].

in the fluid and on the surface, respectively. Consequently, $k_y = k_0 \sin\theta_r$ and $k_z = k_0 \cos\theta_r$ with $k_0 = 2\pi f / c_0$.

Assuming a harmonic time dependence, the two travelling bulk acoustic waves can be described by the velocity potential

$$\begin{aligned}\phi_1 &= \frac{u_0}{k}\exp\left(\mathrm{i}\left(-\omega t + k_y y + k_z z\right)\right)\\ &= \frac{u_0}{k}\exp\left(-\mathrm{i}\omega t\right)\exp\left(\mathrm{i}\alpha\right)\\ \phi_2 &= \frac{u_0}{k}\exp\left(\mathrm{i}\left(-\omega t - k_y y + k_z z\right)\right)\\ &= \frac{u_0}{k}\exp\left(-\mathrm{i}\omega t\right)\exp\left(\mathrm{i}\psi\right)\end{aligned} \tag{2}$$

where all spatially dependent variables were collected in α and ψ and i is the imaginary unit. The pressure and velocity fields can be obtained as

$$\begin{aligned}p_j &= -\rho_0 \frac{\partial \phi_j}{\partial t}\\ \boldsymbol{v}_j &= \nabla \phi_j\end{aligned} \tag{3}$$

where $j \in \{1,2\}$ and ρ_0 is the equilibrium density of the fluid [20].

2.1 Theory of primary radiation force in surface wave devices

In our previous work [18], we presented an analytical expression for the acoustic radiation force in the horizontal direction within a microchannel. In this section, we expand this theoretical investigation for the vertical direction and validate the horizontal trapping force against a numerical model.

The primary acoustic radiation force of any external field can be obtained generally by

$$\boldsymbol{F}_{\mathrm{rad}} = -\pi a^3 \left[\frac{2\kappa_0}{3}\mathrm{Re}\left[f_1^* p_{\mathrm{in}}^* \nabla p_{\mathrm{in}}\right] - \rho_0 \mathrm{Re}\left[f_2^* \boldsymbol{v}_{\mathrm{in}}^* \cdot \nabla \boldsymbol{v}_{\mathrm{in}}\right]\right]$$

with

$$\begin{aligned}f_1\left(\kappa_i\right) &= 1 - \kappa_{\mathrm{p}}/\kappa_0\\ f_2\left(\tilde{\rho}, \tilde{\delta}\right) &= \frac{2\left[1-\gamma\left(\tilde{\delta}\right)\right]\left(\tilde{\rho}-1\right)}{2\tilde{\rho}+1-3\gamma\left(\tilde{\delta}\right)}\\ \gamma\left(\tilde{\delta}\right) &= -\frac{3}{2}\left[1+\mathrm{i}\left[1+\tilde{\delta}\right]\right]\tilde{\delta}\end{aligned} \tag{4}$$

where $\tilde{\rho} = \rho_{\mathrm{p}}/\rho_0$ is the density ratio of the particle and the medium and κ_{p} and κ_0 are the compressibilities of the particle and the medium, respectively [21].

The primary radiation force due to standing surface waves can be obtained by substituting into Eq. (4) the pressure and velocity fields given by Eqs. (2) and (3). In the horizontal y direction both $p_{\mathrm{in}}^* \nabla p_{\mathrm{in}}$ and $\boldsymbol{v}_{\mathrm{in}}^* \cdot \nabla \boldsymbol{v}_{\mathrm{in}}$ are pure real, therefore the force has two terms:

$$F_{\mathrm{rad},y} = F_{y0}\left[f_1 + \frac{3}{2}\mathrm{Re}\left[f_2\right]\frac{k_y^2 - k_z^2}{k_0^2}\right]\sin\left(2k_y y\right)$$

or equivalently

$$F_{\mathrm{rad},y} = F_{y0}\left[f_1 - \frac{3}{2}\mathrm{Re}\left[f_2\right]\cos 2\theta_r\right]\sin\left(2k_y y\right) \tag{5}$$

with

$$F_{y0} = V_{\mathrm{p}} E_{\mathrm{ac}} k_y$$

The force reduces to the one valid for bulk standing waves, when $k_y = k_0$ and $k_z = 0$. Furthermore, the force is zero when $k_y = 0$ and $k_z = k_0$, which would be the case for two upwards directed travelling waves.

For the vertical z direction, the pressure component $p_{\mathrm{in}}^* \nabla p_{\mathrm{in}}$ is pure imaginary, and as the monopole scattering coefficient f_1 is pure real, the first term vanishes, leaving only

$$F_{\mathrm{rad},z} = F_{\mathrm{rad},0}\left[1 - \frac{k_y^2 - k_z^2}{k_0^2}\cos\left(2k_y y\right)\right]$$

or

$$F_{\mathrm{rad},z} = F_{\mathrm{rad},0}\left[1 + \cos 2\theta_r \cos\left(2k_y y\right)\right] \tag{6}$$

with

$$F_{\mathrm{rad},0} = 2\pi a^3 k_z u_0^2 \rho_0 \,\mathrm{Im}\left[f_2\right]$$

This force is trivially zero, when the two travelling waves are along y as $k_y = k_0$ and $k_z = 0$. For the case of two upwards travelling waves, $k_y = 0$ and $k_z = k_0$, resulting in $F_{\mathrm{rad},z} = 4\pi a^3 \rho_0 u_0^2 \mathrm{Im}\left[f_2\right]$, which is analogous to the superposition of two travelling waves [21].

2.2 Finite element validation of the horizontal radiation force

To validate the proposed form of the primary acoustic radiation force in the horizontal direction within the device, the structure was modeled in a finite element numerical simulation (COMSOL Multiphysics AB, Sweden). The simulation domain comprised a rectangular fluid domain, surrounded by a perfectly matched layer, as shown in Fig. 2. The width was λ_y, so two pressure nodes were present in the device in the y direction, and the height was λ_0 to allow for more pressure nodes in the vertical direction. The thickness of the perfectly matched layer (PML) was tenth of the wavelength in the fluid domain $\left(\lambda_0/10\right)$. The

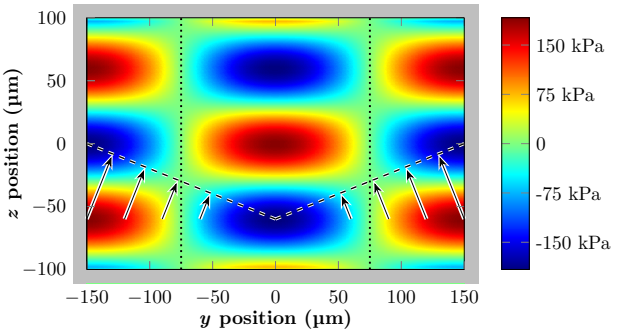

Fig. 2 The pressure distribution within the microchannel. The grey edges symbolize the perfectly matched layer domain. Slanted dashed lines denote the wavefronts of the two travelling BAW waves, with constant phase. The travelling waves have 22° angle with the *z* axis. The particles with positive contrast trap at the pressure nodes, denoted by vertical dotted lines

only boundary conditions were hard wall boundaries at the outer PML edges. The pressure fields were directly applied by background pressure fields, with propagation wave vectors $\boldsymbol{k}_1 = k_y\hat{\boldsymbol{y}} + k_z\hat{\boldsymbol{z}}$ and $\boldsymbol{k}_2 = -k_y\hat{\boldsymbol{y}} + k_z\hat{\boldsymbol{z}}$. To have an accurate resolution with respect to the frequency domain study, the mesh size was maximized at $\lambda_0/6$, which resulted in 45,000 degrees of freedom. To validate the model, we indicated a constant phase wavefront for both travelling waves in the simulation. The propagating waves (perpendicular arrows) have indeed 22° angle with the vertical *z* axis.

After generating the pressure field within the device (see Fig. 2), the radiation force was calculated using Gorkov's potential approach [17]:

$$\begin{aligned} U_{\text{rad}} &= V_{\text{p}}\left[f_1 \frac{1}{2\rho_0 c_0^2} p^2 - f_2 \frac{3}{4}\rho_0 \left\langle \boldsymbol{v}_{\text{in}} \cdot \boldsymbol{v}_{\text{in}} \right\rangle \right] \\ \boldsymbol{F}_{\text{rad}} &= -\nabla U_{\text{rad}} \\ f_1 &= 1 - \kappa_{\text{p}}/\kappa_0 \\ f_2 &= \frac{2\left(\rho_p - \rho_0\right)}{2\rho_p + \rho_0} \end{aligned} \tag{7}$$

Although the dipole scattering factors given in the theory and in this section are different, on the scale of our manipulation frequencies and particles, the normalized viscous boundary layer evaluates to $\tilde{\delta} \approx 0.03$, and therefore the imaginary part of f_2 would be negligible. Moreover, according to the theory, in the horizontal direction only the real part plays a role. Therefore, the above equations can capture the radiation force accurately.

The radiation force was calculated using the theoretical equation, the above numerical model, and as a reference, we calculated the radiation force in a same amplitude BAW device. Two types of particles were investigated: polystyrene (PS), which has similar density to water, and iron-oxide, which is quite different to water both by density and compressibility. The entire list of simulation parameters can be seen in Table 1. The results are plotted in Fig. 3. For both particles, there is excellent agreement between the COMSOL numerical model and our theoretical prediction. The contrast factors for the bulk case and surface wave case differ in the term depending on the dipole scattering coefficient. As they are a function of density difference of particle and fluid, the small difference for PS bulk radiation force and surface wave radiation force is explained, since in this case the density ratio is 1.05. Using the same reasoning, a larger difference is expected in the case of the iron-oxide particle which has a ratio of 1.5. This difference is shown in Fig. 3. The peak primary radiation force and acoustic contract factor are reported in Table 2. The ratio of $F_{y,\text{SAW}}$ to $F_{y,\text{BAW}}$ is equal to the ratio of the contrast factor, $\Phi_{\text{SAW}}/\ \Phi_{\text{BAW}}$. Therefore, we successfully validated our proposed force equation and theoretical predictions in the horizontal direction of a standing surface acoustic wave.

Table 1 Parameters used in the numerical simulation. Values marked with a star (*) are calculated based on other parameters and are presented to aid the reader

Symbol	Description	Value
f	Frequency	13.3 MHz
c_0	Speed of sound in water	1480 m/s
c_s	Speeed of sound on the lithium niobate surface	3990 m/s
λ_0	Wavelength in water*	111.28 μm
λ_s	Wavelength on surface*	300 μm
θ_r	Rayleigh radiation angle*	21.77°
	Width of channel	λ_s=300 μm
	Height of channel	
p_0	Pressure amplitude	96 kPa
ρ_0	Density of water	998 kg/m^3
ρ_{PS}	Density of PS particle	1050 kg/m^3
ρ_{FeO}	Density of FeO particle	1500 kg/m^3
κ_0	Compressibility of water	457 TPa^{-1}
κ_{PS}	Compressibility of PS particle	249 TPa^{-1}
κ_{FeO}	Compressibility of FeO particle	6.67 TPa^{-1}
$f_{1,\text{PS}}$	Monopole scattering coefficient of PS particle*	0.455
$f_{2,\text{PS}}$	Dipole scattering coefficient of PS particle*	0.034
$f_{1,\text{FeO}}$	Monopole scattering coefficient of FeO particle*	0.985
$f_{2,\text{FeO}}$	Dipole scattering coefficient of FeO particle*	0.251

Table 2 Summary of bulk and surface wave contrast factor of particles (PS: polystyrene, FeO: iron-oxide) and the resulting peak primary acoustic radiation force by theory ($F_{y,\mathrm{BAW}}$ and $F_{y,\mathrm{SAW}}$) and simulations ($F_{y,\mathrm{sim}}$). The forces are in pN

	Φ_{BAW}	Φ_{SAW}	$F_{y,\mathrm{BAW}}$	$F_{y,\mathrm{SAW}}$	$F_{y,\mathrm{sim}}$	Reduction
PS	0.51	0.42	23.4	19.4	19.4	17%
FeO	1.36	0.71	63	32.9	32.9	48%

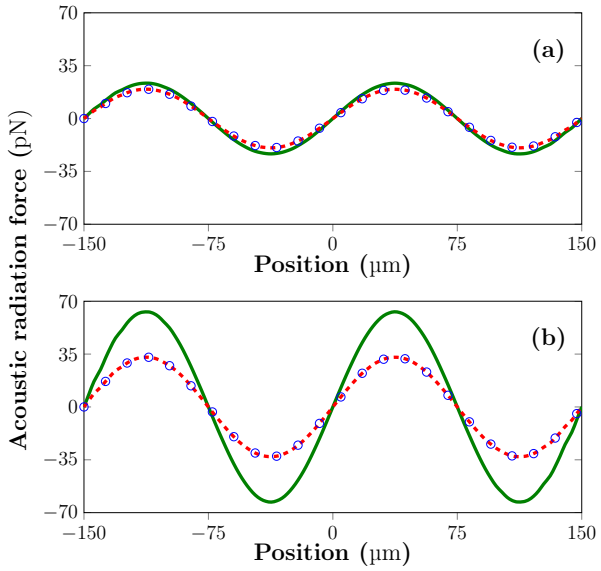

Fig. 3 Comparison of primary acoustic radiation force for a bulk device (solid green), our modified theory (red dashed) and the COMSOL numerical simulation (blue circles) for (a) a polystyrene particle (b) and iron-oxide particle. The larger difference for the iron-oxide particle is due to the more pronounced dependence on density with the surface wave radiation force

3 The phase modulated sorting technique

In a microchannel filled with a fluid, the suspended particles experience the hydrodynamic drag force in addition to the acoustic force. The viscous force is given as

$$F_{\mathrm{drag}} = -6\pi\eta a\dot{y} = -c_{\mathrm{visc}}\dot{y} \tag{8}$$

where η is the dynamic viscosity of the medium and a is the radius of the particle. The radiation force scales with the particle volume while the viscous force scales with particle radius. Therefore, different size particles are subject to different magnitude of radiation and viscous forces and this can be utilized for sorting.

The illustration of our sorting method can be seen in Fig. 4. Particles or cells are initially located at the bottom pressure node inside the channel, where they are naturally trapped due to their positive contrast factor [left of Fig. 4(c)]. The utilized phase pattern is shown in Fig. 4(a). First, the phase is ramped linearly from 0° to 360° at a

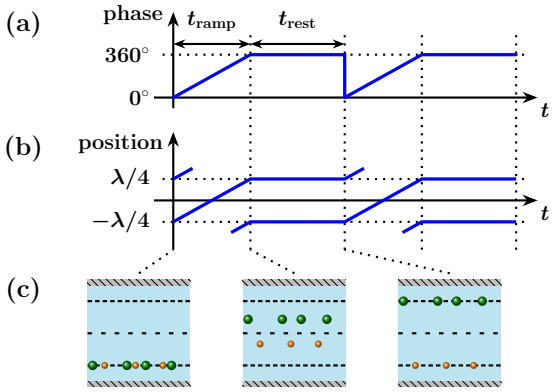

Fig. 4 Illustration of the phase modulated sorting method. (a) the phase pattern used on the second transducer (b) the resulting movement of the nodes (c) the particle distribution in the microchannel at different time instants

rate that displaces the small and large particles at different speeds, such that they are located on different sides of the pressure antinode after the ramping time t_{ramp} [Fig. 4(c) middle graph]. As the primary radiation force will make them relax towards the nearest pressure node during the resting period, t_{rest}, where the phase is kept constant, they locate at a different spatial location, and separation can be achieved [Fig. 4(c) right graph]. As the radiation force is also density-dependent, particles with different density can be separated as well.

4 Phase modulated trajectories

In this section, we derive an analytical expression for the particle trajectories followed by the expansion of the COMSOL model by a time domain simulation to obtain the numerical particle trajectories. We also describe the setup for obtaining the experimental particle trajectories. Finally, results are presented for density-based sorting to show a threefold agreement between theory, simulation and experiment.

4.1 Analytical trajectories describing particle motion in phase modulated fields

The analytical particle trajectories in phase modulated fields can be obtained by balancing the primary radiation force with the viscous drag force [16]:

$$F_{\mathrm{rad},y} = -F_{\mathrm{visc}} \tag{9}$$

In phase modulated fields, when the modulation speed s, given by the time derivative of the phase, is much less than the frequency of the signal $(s \ll \omega)$, the modulation simply enters the argument of the sin() in the force equation [18]:

$$F_{\mathrm{rad},y} = c_{\mathrm{ac}} \sin\left(2k_y y - s\left(t - t_{\mathrm{s}}\right)\right) \tag{10}$$

assuming now that we have a linear phase shift $s = 2\pi/t_{\mathrm{ramp}}$ and t_{s} denotes the start of the phase shift. The force balance can be solved using substitutional integration, and

$$y(t) = \frac{s\left(t - t_s\right)}{2k_y} + \frac{1}{k_y}\tan^{-1}\left[\left[\gamma - Q\tan\left(\frac{Q}{2}\left(c_1 + t\right)\right)\right]\Big/ s\right] \tag{11}$$

where $Q = \sqrt{s^2 - \gamma^2}$ and $\gamma = 2k_y c_{\mathrm{ac}}/c_{\mathrm{visc}}$ and c_1 is a constant satisfying the initial conditions for particle position and the $\tan^{-1}[]$ function in Eq. (11) has to be normalized to be monotonic on the solution time range. We note the change of the reference point within the coordinate system with respect to our previous work [18].

4.2 Numerical model

Numerical simulations of the particle motion are carried out in COMSOL. The previous model, that was used for the force approximation was combined with the particle-tracking module to calculate the particles trajectories. The simulation process is schematically illustrated in Fig. 5. As the phase modulation cannot be implemented in a continuous manner, it had to be discretized: the ramping cycle is divided into ten steps, from 18° to 342°, each step being 36°. For each phase step the pressure distribution is generated and stored, which are utilized by a time domain simulation implemented with the particle tracing module. The particles are placed at the pressure node on the left (at $y = -\lambda_s/4 = -75$ µm) at $t = 0$ s . The particles are assumed to be subjected to two forces: the primary radiation force, which is calculated using the stored frequency domain results of the pressure and acoustic velocity fields,

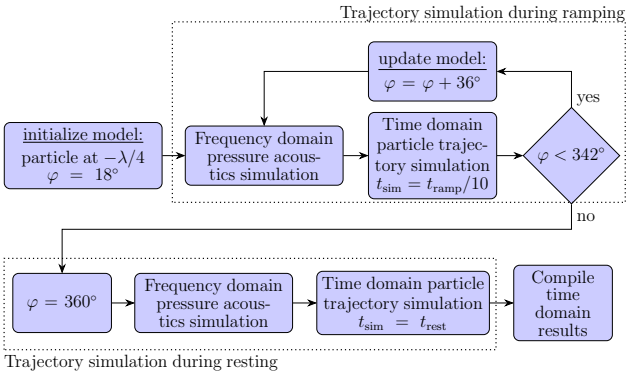

Fig. 5 Flowchart of the time domain trajectory simulation in COMSOL Multiphysics

and the viscous drag force. No gravity or buoyancy force is included as the primary focus is on obtaining the horizontal forces and particle movement. Once the ramping cycle is simulated, the rest period is generated using a frequency domain result for 0°. Finally, the partial results are collated, and the final trajectories are saved.

4.3 Experimental setup

The manufacturing steps of the device comprising the lithium niobate substrate and PDMS microchannel are presented in detail elsewhere [19]. The particle mixture was prepared by mixing 20 µl of iron-oxide and polystyrene particle suspension with 10 ml of 30 % iodixanol solution (OptiPrep, SigmaAldrich, UK and DI water) to prevent heavy particles from sinking to the channel bottom. The signal generator (TG5012A, Aim-TTi, UK) is driven via a USB connection from the PC using LabView (National Instruments, UK). The initial phase of the second transducer is adjusted to achieve the symmetric node distribution within the channel (Fig. 4c). The 13.3 MHz ultrasound signals are amplified using two high-power amplifiers (ZHL-1-2W+, Mini-Circuits, UK). The data acquisition is performed by a bright field microscope (Olympus BX51, Olympus, UK) and camera (Orca Flash 2.8, Hamamatsu, UK). Finally, the obtained recordings are post-processed by Tracker (Douglas Brown, https://physlets.org/tracker/) to extract the particle trajectories. Each experiment was carried out 5 times.

4.4 Comparison results of trajectories for synthetic particles

Theoretical and simulation validation of experiments can be seen in Fig. 6. The only fitting parameter for the theoretical/simulation results was the acoustic pressure amplitude. To complement size-based trajectory results presented in [18], here density-based sorting of iron-oxide filled and polystyrene particles of 10 µm diameter was carried out with good agreement with R^2 value of 0.9193.

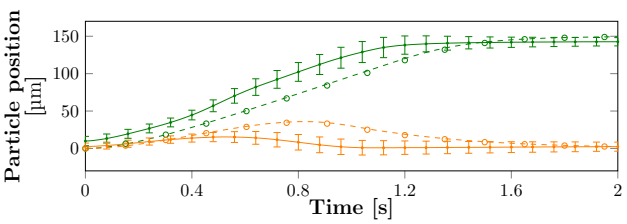

Fig. 6 Theoretical (dashed), simulation (circles) and experimental (continuous lines and error bars) particle trajectories. Green and orange color corresponds to iron-oxide and polystyrene particles, respectively. The error bars show standard deviation of five experiments

We attribute the small difference between experimental and theoretical/simulation results to the unknown speed of sound of the media due to the OptiPrep density gradient used. When the speed of sound due to the increased density is assumed to be increased by 10%, the R^2 value of the fit increases to 0.9613. As the heavier particles are iron-oxide filled polystyrene particles, their density and compressibility are difficult to characterize precisely that can also lead to uncertainties in the theoretical fit. Generally, any parameter change that results in the ratio of the acoustic contrast factor of the PS and iron-oxide filled particles to be decreased improves the fit. For effect of other parameters on particle trajectories and sensitivity analysis of acoustic sorting methods refer to [22].

5 Summary

We demonstrated that the primary acoustic radiation force in a standing surface wave device is different to the one valid in bulk standing wave fields. Numerical modelling of this force using COMSOL simulation validated our theory in the horizontal direction within the microchannel. Analytical particle trajectories are obtained by balancing the primary radiation force with the viscous drag force. Expanding the COMSOL model with a time domain simulation allows for numerical generation of particle trajectories. Moreover, the analytical and numerical approaches were validated experimentally by measuring the trajectories of iron-oxide and polystyrene particles in a microfluidic surface acoustic wave device.

Acknowledgements

The authors thank Mr Neil Ross for help with the cleanroom fabrication and Dr William N MacPherson for access to thermal evaporator equipment. We are grateful to Mr Gergely Hantos for presenting a shorter version of this paper as a talk at the First Symposium on Smart Systems Integration.

Nomenclature

SAW	surface acoustic wave
SSAW	standing surface acoustic wave
BAW	bulk acoustic wave
LSAW	leaky surface acoustic wave
a	radius of the particle
c_0	speed of sound in the fluid
c_s	surface acoustic wave velocity on the lithium niobate substrate
E_{ac}	acoustic energy density
f	frequency
f_1	monopole scattering coefficient
f_2	dipole scattering coefficient
$\boldsymbol{F}_{\mathrm{rad}}$	Acoustic radiation force
$\boldsymbol{F}_{\mathrm{rad},\,y}$	acoustic radiation force in the y-direction
$\boldsymbol{F}_{\mathrm{rad},\,z}$	acoustic radiation force in the z-direction
$\boldsymbol{k}$	wave vector
k	wavenumber or magnitude of the wave vector
k_y	y-component of the wave vector
k_z	z-component of the wave vector
p_{in}	incident acoustic pressure field
t	time
t_{ramp}	ramping time
t_{rest}	resting time
v_{in}	incident velocity field
V_{p}	particle volume
x, y, z	cartesian coordinates
η	dynamic viscosity of the fluid
θ_{r}	refraction angle
κ_0	compressibility of the fluid medium
κ_p	compressibility of the particle
λ_0	wavelength in the fluid medium
ρ_0	density of the fluid medium
ρ_{p}	density of the particle
Φ_{AC}	acoustic contrast factor
ω	Angular frequency

References

[1] Bruus, H. "Theoretical Microfluidics", Oxford University Press, UK, 2008.

[2] Yildiz-Ozturk, E., Yesil-Celiktas, O. "Diffusion phenomena of cells and biomolecules in microfluidic devices", Biomicrofluidics, 9(5), pp. 052606, 2015. https://doi.org/10.1063/1.4923263

[3] Di Carlo, D., Irimia, D., Tompkins, R. G., Toner, M. "Continuous inertial focusing, ordering, and separation of particles in microchannels", Proceedings of the National Academy of Sciences of the United States of America, 104(48), pp. 18892–18897, 2007. https://doi.org/10.1073/pnas.0704958104

[4] Guttenberg, Z., Muller, H., Habermuller, H., Geisbauer, A., Pipper, J., Felbel, J., Kielpinski, M., Scriba, J., Wixforth, A. "Planar chip device for PCR and hybridization with surface acoustic wave pump", Lab on a Chip, 5(3), pp. 308–317, 2005. https://doi.org/10.1039/b412712a

[5] Shields, C. W., Reyes, C. D., Lopez, G. P. "Microfluidic cell sorting: a review of the advances in the separation of cells from debulking to rare cell isolation", Lab on a Chip, 15(5), pp. 1230–1249, 2015. https://doi.org/10.1039/c4lc01246a

[6] Tanaka, T., Ishikawa, T., Numayama-Tsuruta, K., Imai, Y., Ueno, H., Matsuki, N., Yamaguchi, T. "Separation of cancer cells from a red blood cell suspension using inertial force", Lab on a Chip, 12(21), pp. 4336–4343, 2012.
https://doi.org/10.1039/c2lc40354d

[7] Ohlsson, P., Evander, M., Petersson, K., Mellhammar, L., Lehmusvuori, A., Karhunen, U., Soikkeli, M., Seppa, T., Tuunainen, E., Spangar, A., von Lode, P., Rantakokko-Jalava, K., Otto, G., Scheding, S., Soukka, T., Wittfooth, S., Laurell, T. "Integrated Acoustic Separation, Enrichment, and Microchip Polymerase Chain Reaction Detection of Bacteria from Blood for Rapid Sepsis Diagnostics", Analytical Chemistry, 88(19), pp. 9403–9411, 2016.
https://doi.org/10.1021/acs.analchem.6b00323

[8] Bruijns, B., van Asten, A., Tiggelaar, R., Gardeniers, H. "Microfluidic Devices for Forensic DNA Analysis: A Review", Biosensors (Basel), 6(3), pp. 41, 2016.
https://doi.org/10.3390/bios6030041

[9] Wei Hou, H., Gan, H. Y., Bhagat, A. A., Li, L. D., Lim, C. T., Han, J. "A microfluidics approach towards high-throughput pathogen removal from blood using margination", Biomicrofluidics, 6(2), pp. 24115–2411513, 2012.
https://doi.org/10.1063/1.4710992

[10] Lenshof, A., Laurell, T. "Continuous separation of cells and particles in microfluidic systems", Chemical Society Reviews, 39(3), pp. 1203–1217, 2010.
https://doi.org/10.1039/b915999c

[11] Ji, H. M., Samper, V., Chen, Y., Heng, C. K., Lim, T. M., Yobas, L. "Silicon-based microfilters for whole blood cell separation", Biomedical Microdevices, 10(2), pp. 251–257, 2008.
https://doi.org/10.1007/s10544-007-9131-x

[12] Hulett, H. R., Bonner, W. A., Barrett, J., Herzenberg, L. A. "Cell Sorting: Automated Separation of Mammalian Cells as a Function of Intracellular Fluorescence", Science, 166(3906), pp. 747–749, 1969.
https://doi.org/10.1126/science.166.3906.747

[13] Glynne-Jones, P., Hill, M. "Acoustofluidics 23: acoustic manipulation combined with other force fields", Lab on a Chip, 13(6), pp. 1003–1010, 2013.
https://doi.org/10.1039/c3lc41369a

[14] Di Carlo, D. "Inertial microfluidics", Lab on a Chip, 9(21), pp. 3038–3046, 2009.
https://doi.org/10.1039/b912547g

[15] Wiklund, M. "Acoustofluidics 12: Biocompatibility and cell viability in microfluidic acoustic resonators", Lab on a Chip, 12(11), pp. 2018–2028, 2012.
https://doi.org/10.1039/c2lc40201g

[16] Bruus, H. "Acoustofluidics 7: The acoustic radiation force on small particles", Lab on a Chip, 12(6), pp. 1014–1021, 2012.
https://doi.org/10.1039/c2lc21068a

[17] Gorkov, L. P. "On the forces acting on a small particle in an acoustic field in an ideal fluid", Soviet Physics Doklady, 6(9), pp. 773–775, 1962.

[18] Simon, G., Andrade, M. A. B., Reboud, J., Marques-Hueso, J., Desmulliez, M. P. Y., Cooper, J. M., Riehle, M. O., Bernassau, A. L. "Particle separation by phase modulated surface acoustic waves", Biomicrofluidics, 11(5), pp. 054115, 2017.
https://doi.org/10.1063/1.5001998

[19] Simon, G., Pailhas, Y., Andrade, M. A. B., Reboud, J., Marques-Hueso, J., Desmulliez, M. P. Y., Cooper, J. M., Riehle, M. O., Bernassau, A. L. "Particle separation in surface acoustic wave microfluidic devices using reprogrammable, pseudo-standing waves", Applied Physics Letters, 113(4), pp. 2018.
https://doi.org/10.1063/1.5035261

[20] Kinsler, L. E., Frey, A. R., Coppens, A. B., Sanders, J. V. "4th ed. "Fundamentals of Acoustics", Wiley, 1999.

[21] Settnes, M., Bruus, H. "Forces acting on a small particle in an acoustical field in a viscous fluid", Physical Review E, 85(1 Pt 2), pp. 016327, 2012.
https://doi.org/10.1103/PhysRevE.85.016327

[22] Simon, G., Hantos, B. G., Andrade, M. A. B., Desmulliez, M. P. Y., Riehle, M. O., Bernassau, A. L. "Monte-Carlo based sensitivity analysis of acoustic sorting methods", Periodica Polytechnica Electrical Engineering and Computer Science, 2019.
https://doi.org/10.3311/PPee.13455